

## Research Article

# Study on an Undershot Cross-Flow Water Turbine with Straight Blades

Yasuyuki Nishi,<sup>1</sup> Terumi Inagaki,<sup>1</sup> Yanrong Li,<sup>1</sup> and Kentaro Hatano<sup>2</sup>

<sup>1</sup>Department of Mechanical Engineering, Ibaraki University, 4-12-1 Nakanarusawa-cho, Hitachi-shi, Ibaraki 316-8511, Japan

<sup>2</sup>Graduate School of Science and Engineering, Ibaraki University, 4-12-1 Nakanarusawa-cho, Hitachi-shi, Ibaraki 316-8511, Japan

Correspondence should be addressed to Yasuyuki Nishi; [y-nishi@mx.ibaraki.ac.jp](mailto:y-nishi@mx.ibaraki.ac.jp)

Received 31 March 2015; Revised 13 June 2015; Accepted 15 June 2015

Academic Editor: Ryoichi Samuel Amano

Copyright © 2015 Yasuyuki Nishi et al. This is an open access article distributed under the Creative Commons Attribution License, which permits unrestricted use, distribution, and reproduction in any medium, provided the original work is properly cited.

Small-scale hydroelectric power generation has recently attracted considerable attention. The authors previously proposed an undershot cross-flow water turbine with a very low head suitable for application to open channels. The water turbine was of a cross-flow type and could be used in open channels with the undershot method, remarkably simplifying its design by eliminating guide vanes and the casing. The water turbine was fitted with curved blades (such as the runners of a typical cross-flow water turbine) installed in tube channels. However, there was ambiguity as to how the blades' shape influenced the turbine's performance and flow field. To resolve this issue, the present study applies straight blades to an undershot cross-flow water turbine and examines the performance and flow field via experiments and numerical analyses. Results reveal that the output power and the turbine efficiency of the Straight Blades runner were greater than those of the Curved Blades runner regardless of the rotational speed. Compared with the Curved Blades runner, the output power and the turbine efficiency of the Straight Blades runner were improved by about 31.7% and about 67.1%, respectively.

## 1. Introduction

As environmental and energy problems become critical, small-scale hydroelectric power generation is attracting significant attention as a means of utilizing natural energy. Water turbines used for small-size hydroelectric power generation are largely categorized into the tube channel-type [1–3] (including the Francis and propeller water turbines) and open channel-type [4–6]. Tube channel water turbines require relatively large heads, resulting in a decrease in the number of suitable construction sites, whereas open channel water turbines require almost no attached facility, enabling their direct installation in open channels, thus being environmentally friendly and easier to maintain. Accordingly, open channel water turbines have been applied in small-to-medium rivers and irrigation canals at numerous sites. However, as these water turbines have been primarily designed for motive power, their design style is not yet well established; for example, they are of large size and have low turbine efficiency.

Considering these circumstances, the authors aimed to develop a water turbine with a very low head that was suitable for application to open channels; thus, an undershot cross-flow water turbine [7, 8] was proposed. Compared with cross-flow water turbines [9, 10] with medium-to-low heads applied to tube channels, the proposed water turbine offered a greatly simplified design thanks to its lack of guide vanes and the casing, and it was applied to open channels with the undershot method. It was revealed [7, 8] that the proposed water turbine, unlike conventional undershot water turbines, did not whirl the water with its blades and thus did not accumulate air bubbles between them. It also received the flow twice owing to the through-flow effect, thereby greatly improving the turbine efficiency. Furthermore, the water turbine's flow field with a free surface was elucidated by particle image velocimetry measurement and numerical analyses [11, 12]. However, since the water turbine used curved blades such as the runners of a typical cross-flow water turbine used for tube channels, the effect of the blade's shape on the performance and flow field was unclear.

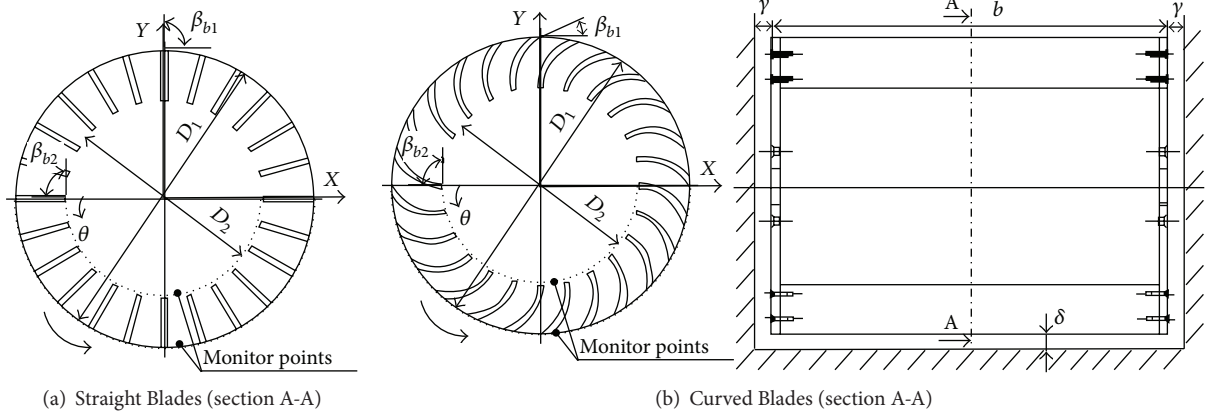


FIGURE 1: Test runners.

TABLE 1: Specifications of test runners.

	Straight Blades	Curved Blades
Outer diameter: $D_1$		0.18 m
Inner diameter: $D_2$		0.12 m
Inlet angle: $\beta_{b1}$	90°	30°
Outlet angle: $\beta_{b2}$		90°
Runner width: $b$		0.24 m
Side clearance: $\gamma$		5 mm
Bottom clearance: $\delta$		5 mm
Number of blades: $Z$		24

This study applies straight blades to an undershot cross-flow water turbine and examines the performance and flow field through experiments and numerical analyses.

## 2. Experimental Apparatus and Method

Two types of test runners used in this study are illustrated in Figures 1(a) and 1(b), and their specifications are presented in Table 1. Figure 1(a) shows another prototype runner whose original curved blades are replaced by radially arranged straight blades, hereafter referred to as the Straight Blades runner. Figure 1(b) shows a prototype runner based on a cross-flow runner [10] used for tube channels; hereafter, this prototype is referred to as the Curved Blades runner. The only difference between the two types of runners is the shape of the blades. Both runners have an outer diameter  $D_1$  of 180 mm, runner width  $b$  of 240 mm, side clearance  $\gamma$  of 5 mm, and bottom clearance  $\delta$  of 5 mm. Other specifications for this runner were determined in reference to a typical cross-flow runner [10] used in conjunction with a penstock. The circumferential angle  $\theta$  defined the negative direction of the  $x$ -axis as  $\theta = 0^\circ$  and the counterclockwise rotation as positive. Two velocity-monitoring points were established: one was set at a point 0.5 mm radially outward for the outer periphery of the runners, while the other was set at a point 0.5 mm radially inward for the inner periphery of the runners.

A summarized illustration of the experimental apparatus is shown in Figure 2. The equipment used in this experiment

consisted of an open-air circulation water tank that was used to simulate an open channel. The experiment was conducted with a constant flow rate ( $Q = 0.003 \text{ m}^3/\text{s}$ ), which was measured with an electromagnetic flowmeter. The load on the water turbine was altered using a load machine, and the rotational speed  $n$  and torque  $T$  were measured using a magnetolectric-type rotation detector and a torque meter, respectively, from which we obtained the output power  $P$ . Water depth was measured at 2 points, upstream and downstream from the runner, providing for an upstream water depth  $h_3$  and a downstream water depth  $h_4$ . These depths were derived through measurements obtained at a distance of  $2D_1$  from the center of the runner in both the upstream and downstream directions. Measurements at each location were obtained from a point on the wall surface and from the center point of the channel having a width  $B = 0.25 \text{ m}$ . In addition, both the upstream and downstream flow velocities,  $v_3$  and  $v_4$ , respectively, were obtained using the measured upstream water depth  $h_3$ , the measured downstream water depth  $h_4$ , and the flow rate  $Q$  via the following equations:

$$v_3 = \frac{Q}{(Bh_3)}, \quad (1)$$

$$v_4 = \frac{Q}{(Bh_4)}.$$

We used a 100 mW semiconductor-excited laser sheet as a light source to visualize the flow around the runner by illuminating the central cross-section of the runner width from the bottom of the runner. The thickness of the laser sheet was approximately 1 mm. In this experiment, we used a digital camera of  $1920 \times 1080$  pixels as the photographic device to take pictures at a shooting speed of 60 fps from a direction that is perpendicular to the central cross-section of the illuminated runner width.

## 3. Numerical Analysis Method and Conditions

This study uses the general thermal fluid analysis code ANSYS-CFX13.0 and analyzes a three-dimensional unsteady flow considering free surfaces. The multiphase flow model is

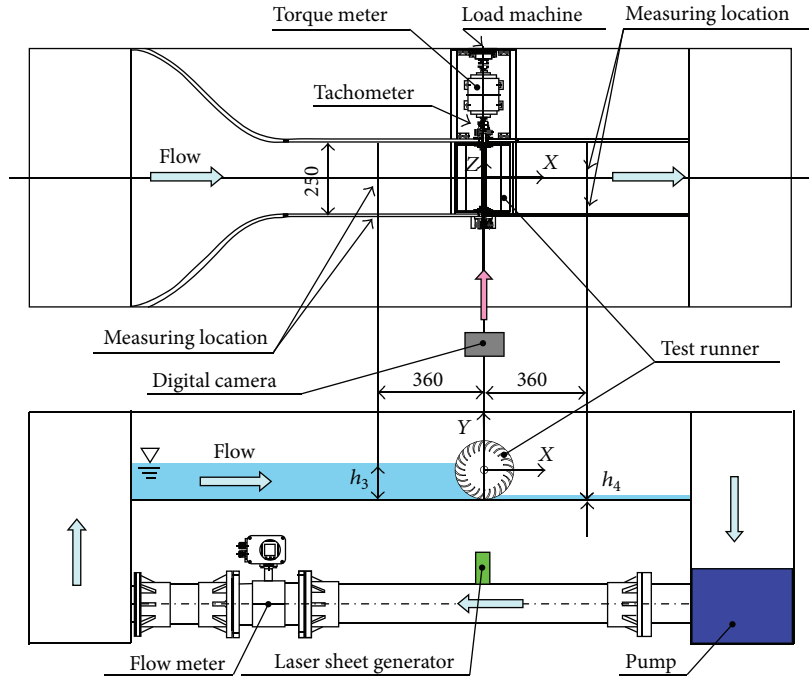


FIGURE 2: Experimental apparatus.

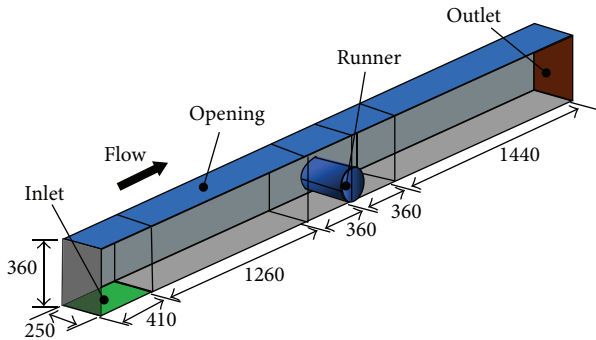


FIGURE 3: Computational domain.

the uniform model [13] of an Euler-Euler simulation, with the acting fluids being water and air. The basic equations used in the model are based upon mass, momentum, and volume conservation [13]. The standard  $k-\varepsilon$  model was adopted as the turbulent flow model, and the standard wall function was used to handle regions near wall surfaces.

The entire computational domain is shown in Figure 3, and the computational grid of each runner is shown in Figures 4(a) and 4(b). The computational domain is composed of the runner and the upstream and downstream domains. The length of the upstream and downstream domains to the center of the runner is  $9D_1$  and  $10D_1$ , respectively. Control surfaces are established at a distance of  $2D_1$  in the upstream and downstream directions from the runner center. The water depth is monitored at these control surfaces as they would be in an experiment. The computational grid of either

runner has about 462 thousand elements and that of both the upstream and downstream has about 420 thousand elements, so the total elements number of the computational grid for either runner is about 882 thousand. To investigate grid dependence, the number of computational grids was increased by approximately 2 times, and analysis was conducted at  $n = 22 \text{ min}^{-1}$ . Although the torque decreased by approximately 3.7% from the result presented in this paper, the effect of computational grid number was comparatively small. For boundary conditions, the mass flow rate was applied to the inlet boundary, free outflow (with a relative air pressure of 0 Pa) was applied to the outlet boundary, and rotational speed was applied to the runner domain. In addition, the top surface of the computational domain was permeable to the atmosphere in order to allow air to move freely in and out of the computational domain, while nonslip conditions were applied to all the other walls. The boundary of the rotational and static domains was joined by the transient rotor-stator method [14]. For initial conditions, the experimental value of the upstream flow velocity  $v_3$  was used as the flow velocity in the simulations. The volume fraction  $VF_{ih}$  of water was defined in accordance with the following formula using the step function:

$$VF_{ih} = \text{step}(h - y). \quad (2)$$

Here,  $y$  is the coordinate of the height direction in the computational domain, and the water depth  $h$  uses the experimental value of the upstream water depth  $h_3$  in the simulations. Therefore, the position  $y \leq h_3$  is the domain of water and the position  $y > h_3$  is the domain of air. In addition, the time step was adjusted to ensure that the runner would

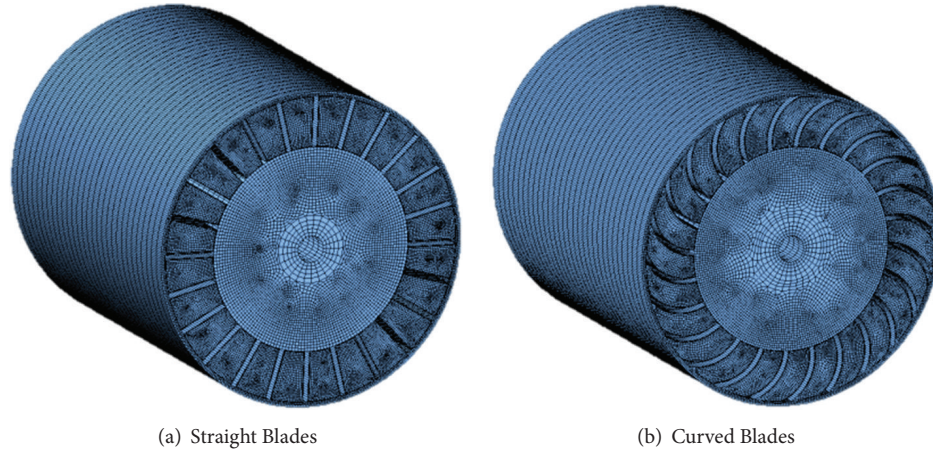


FIGURE 4: Computational grid of the runners.

undergo one rotation every 180 steps, and the time step was recalibrated until fluctuations in the flow became negligible.

#### 4. Experimental and Analysis Results and Considerations

**4.1. Comparison of the Water Turbine Performances.** Figures 5(a)–5(c) present a comparison of the performances of the Straight Blades runner and Curved Blades runner on the basis of the experimental and computational values. For both runners, the computed torque  $T$  reduces as the rotational speed increases. The computed torque  $T$  is greater than its experimental value throughout the rotational speed range. Accordingly, the computed output power  $P$  is greater than the experimental value. However, both computed  $T$  and  $P$  are greater in the case of the Straight Blades runner than in the case of the Curved Blades runner throughout the rotational speed range, and this trend is also seen in the experimental values. The torque with no runner installed is simply measured by rotating the shaft by hand, and the resulting value coincides with the difference between the experimental and computed torque values. Thus, although the difference between the experiment and computation could be attributed to the models of multiphase flow or turbulence, the difference occurs mainly because mechanical friction loss is not taken into consideration in the computation. While the computed turbine efficiency  $\eta$  is greater than its experimental value except in the low rotational speed range, its trend matches the experiment. Comparing the experimental values of both runners, it is revealed that the maximum output power and maximum turbine efficiency of the Straight Blades runner are greater than those of the Curved Blades runner by about 31.7% and about 67.1%, respectively.

A comparison of the time-averaged values of the upstream water depth  $h_3$  and downstream water depth  $h_4$  of the Straight Blades runner and Curved Blades runner from the experiment and computation is shown in Figures 6(a) and 6(b), while a comparison of the time-averaged values of the upstream Froude number  $F_{r3}$  and downstream Froude

number  $F_{r4}$  is shown in Figures 7(a) and 7(b). Here, the upstream Froude number  $F_{r3}$  and the downstream Froude number  $F_{r4}$  are obtained using the following equations, respectively:

$$F_{r3} = \frac{v_3}{\sqrt{gh_3}}, \quad (3)$$

$$F_{r4} = \frac{v_4}{\sqrt{gh_4}}.$$

For both runners, as seen in Figures 6(a) and 6(b), the upstream water depths  $h_3$  from the experiment and computation decrease as the rotational speeds increase; contrarily, the downstream water depths  $h_4$  increase. Furthermore, for both the experiment and computation, the upstream water depths  $h_3$  of the Straight Blades runner are smaller than those of the Curved Blades runner, whereas the downstream water depths  $h_4$  are greater for both runners. This is because the resistance of the runners against the flow decreases as the rotational speed increases, implying that the Straight Blades runner has a smaller resistance than the Curved Blades runner. However, the downstream water depth  $h_4$  from the experiment rapidly increases at around  $n = 16\text{--}19 \text{ min}^{-1}$  for the straight blades runner and  $n = 22\text{--}25 \text{ min}^{-1}$  for the Curved Blades runner, before maintaining a nearly constant value even when the rotational speed further increases. The constant value is about 0.03 m for both runners. As seen in Figure 7(b), the Froude number  $F_{r4}$  from the experiment becomes  $F_{r4} < 1$  at around the point where the downstream water depth  $h_4$  begins to rapidly increase, indicating that the flow has shifted from supercritical to subcritical. Whereas the rotational speeds at which the transition from the supercritical flow to subcritical flow occur differ between the experiment and computation, the water depths and Froude numbers show rather similar values for both runners. Note that the upstream Froude number  $F_{r3}$  from the experiment and computation is always  $F_{r3} < 1$  for both runners, meaning that the flow upstream of the runners is subcritical regardless of the runners' rotational speed.

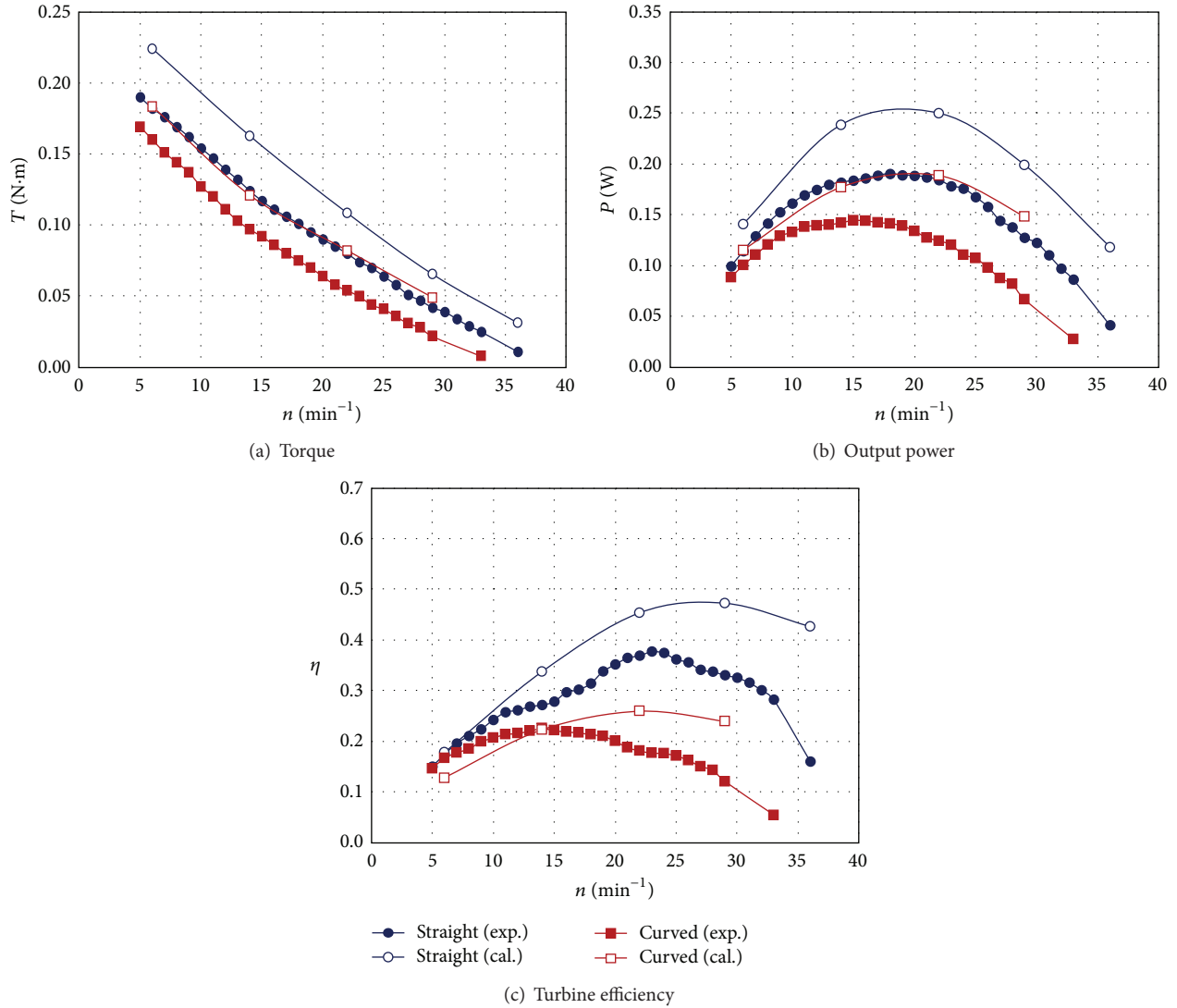


FIGURE 5: Water turbine performance.

From the above findings, this study has demonstrated to a certain extent the qualitative characteristics of the performances and flow fields of water turbines fitted with blades of different shapes.

**4.2. Comparison of Flow Fields.** To compare the flow fields around the Straight Blades runner and Curved Blades runner, the flow field in the middle of the runner width is examined by numerical analyses (described below) at a rotational speed of  $n = 22 \text{ min}^{-1}$  at which the computed output power of both runners roughly becomes maximal.

First, the water-air interfaces are identified with the time-averaged values of the volume fractions of water  $\text{VF}_1$  and  $\text{VF}_2$ , respectively, at the outer and inner circumferences of the Straight and Curved Blades runners, as shown in Figure 8. Here,  $\text{VF} = 1$  is water,  $\text{VF} = 0$  is air, and  $\text{VF} = 0.5$  is an interface of water and air. The water domains of the Straight Blades runner and Curved Blades runner are  $\theta = 27^\circ\text{--}126^\circ$  and  $\theta = 24^\circ\text{--}132^\circ$  and  $\theta = 42^\circ\text{--}114^\circ$  and  $\theta = 57^\circ\text{--}138^\circ$  at the runners'

outer and inner circumferences, respectively, demonstrating that the water domains at both the outer and inner circumferences are narrower on the Straight Blades runner than on the Curved Blades runner.

The velocity triangles [11] of the undershot cross-flow water turbine are shown in Figure 9. Here, the radial component  $v_r$  of the absolute velocity is set positive in the radial inner direction, whereas the circumferential component  $v_u$  is set positive in the rotation direction (counterclockwise rotation). Moreover, the absolute flow angle  $\alpha$  and the relative flow angle  $\beta$  define the rotational direction (counterclockwise rotation) of the runner as positive.

The time-averaged values of the radial component  $v_{r1}$  and circumferential component  $v_{u1}$  of the absolute velocities at the outer circumferences of the Straight and Curved Blades runners are shown in Figures 10(a) and 10(b), whereas the time-averaged values of the radial component  $v_{r2}$  and circumferential component  $v_{u2}$  of the absolute velocities at the inner circumferences of both runners are shown in

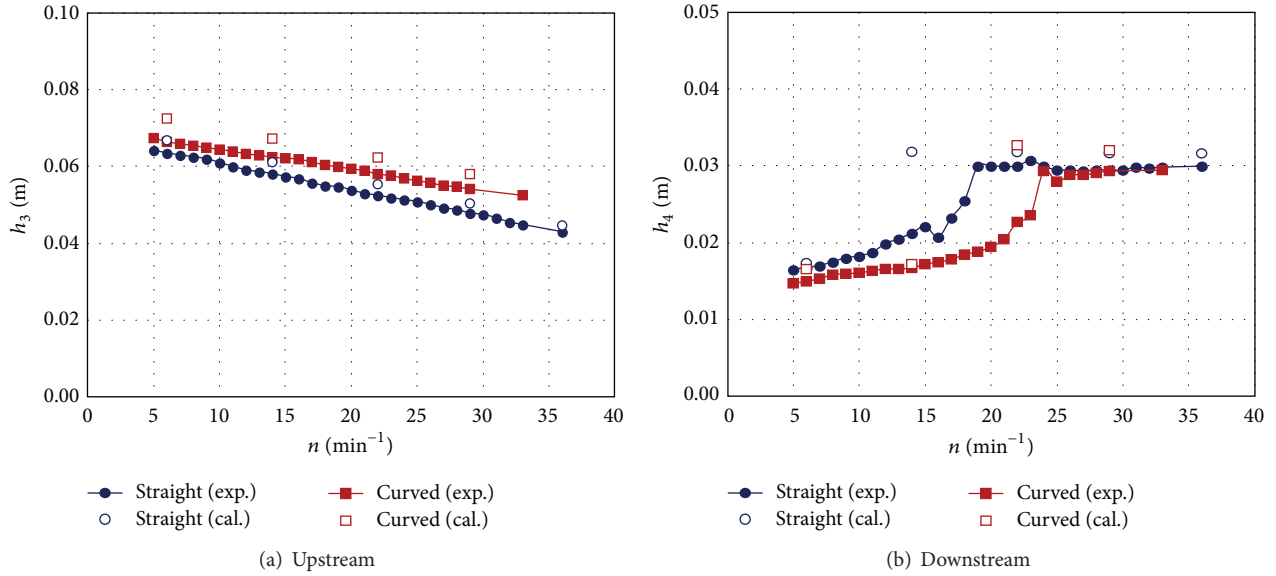


FIGURE 6: Correlation between the rotational speed and both the upstream ( $h_3$ ) and downstream ( $h_4$ ) water depths from experiment and numerical analysis.

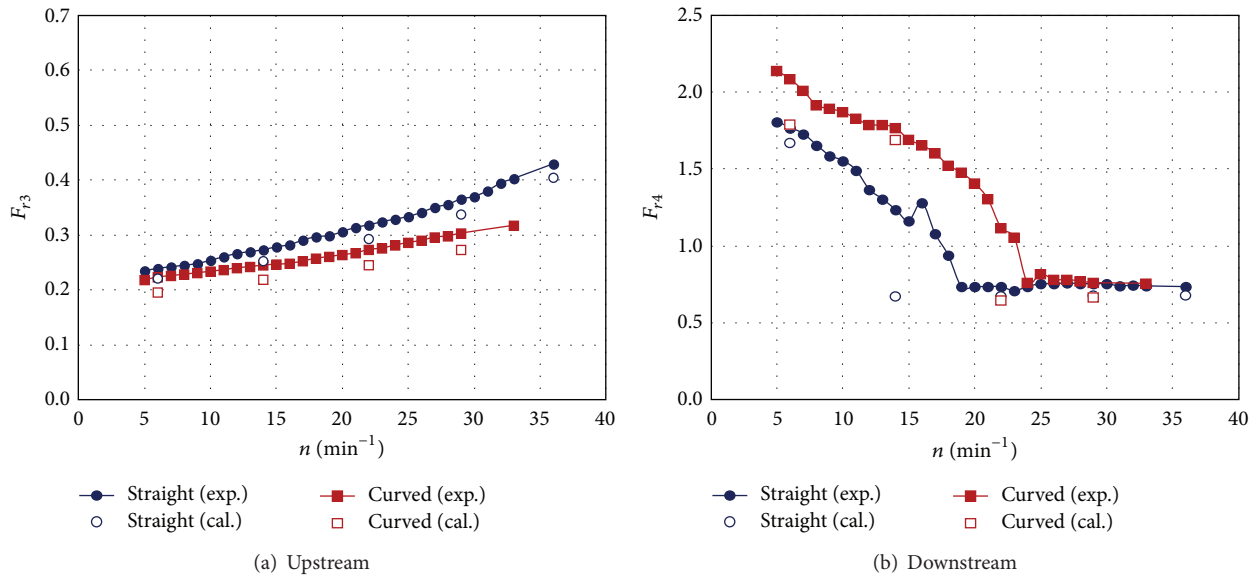


FIGURE 7: Correlation between the rotational speed and both the upstream ( $F_{r3}$ ) and downstream ( $F_{r4}$ ) Froude numbers from experiment and numerical analysis.

Figures 11(a) and 11(b), respectively. Here,  $v_r$  and  $v_u$  of both runners only denote the values in the water domains identified on the basis of the volume fraction of water, as shown in Figure 8. Figure 10(a) shows that the  $v_{r1}$  values of the two runners greatly differ at  $\theta \leq 42^\circ$  and that whereas  $v_{r1}$  of the Curved Blades runner decreases as  $\theta$  decreases,  $v_{r1}$  of the Straight Blades runner increases. This implies that, in the regions with small  $\theta$ , the Straight Blades runner has smaller shock loss and smaller resistance to the flow compared with the Curved Blades runner. At  $\theta > 42^\circ$ ,  $v_{r1}$  of both runners decreases as  $\theta$  increases and turns negative at around  $\theta = 90^\circ$ .

At the outer circumference of the runner,  $v_{r1}$  is positive in the first stage inlet region, and it is negative in the second stage outlet region. These regions are narrower on the Straight Blades runner than on the Curved Blades runner. As seen in Figure 10(b),  $v_{u1}$  of both runners increases as  $\theta$  increases in the first stage inlet region, reaching a maximum at around  $\theta = 87^\circ - 90^\circ$ . However,  $v_{u1}$  of both runners greatly differs in the second stage outlet region; that is,  $v_{u1}$  of the Curved Blades runner decreases as  $\theta$  increases, turning from positive to negative at around  $\theta = 123^\circ$ . Thus, it is conceivable that, in this region, the flow in the Curved Blades runner in the direction

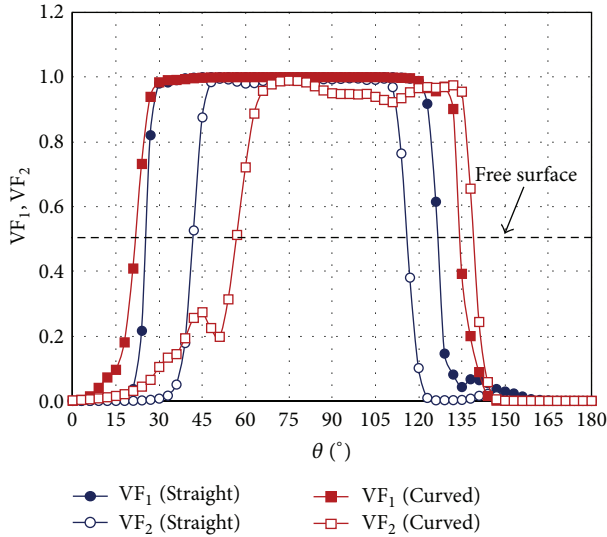


FIGURE 8: Volume fraction of water at the runner's outer ( $VF_1$ ) and inner ( $VF_2$ ) circumferences ( $n = 22 \text{ min}^{-1}$ , cal.).

opposite to the rotation of the runner hinders the reversal flow and leakage flow at the bottom and turns sharply to be against the main flow. Conversely,  $v_{u1}$  of the Straight Blades runner switches from decreasing to increasing at around  $\theta = 117^\circ$ , showing that the flow in the Straight Blades runner is in the same direction as the rotation of the runner and that although there remain swirling flows, the hindrance to the reversal flow and the sharp turn against the main flow are suppressed.

Meanwhile,  $v_{u2}$  decreases as  $\theta$  increases in both Straight blades runner and Curved Blades runner, as shown in Figure 11(a), and turns negative at  $\theta = 90^\circ$  and  $105^\circ$ , respectively. At the inner circumference of the runner,  $v_{r2}$  is positive in the first stage outlet region and is negative in the second stage inlet region. These regions are shifted to lower  $\theta$  values for the Straight Blades runner compared with the Curved Blades runner. Whereas the second stage inlet region is narrower in the case of the Straight Blades runner relative to the Curved Blades runner, the first stage outlet region appears to have almost the same areas for both runners. Figure 11(b) shows that  $v_{u2}$  of the Straight Blades runner is generally greater than that of the Curved Blades runner, especially in the second stage inlet region. Figure 10(b) shows that  $v_{u1}$  of the Straight Blades runner is slightly smaller than that of the Curved Blades runner in the first stage inlet region. Thus, it is conceivable that, in the first stage region, the Straight Blades runner has less swirling flow to enter the second stage outlet than the Curved Blades runner and is unable to sufficiently recover the swirling flow. Therefore, there is apparently a greater amount of swirling flow from the first stage outlet region in the case of the Straight Blades runner than in the case of the Curved Blades runner; part of the flow then locally enters the second stage inlet region. However, as mentioned earlier, since the Straight Blades runner has part of the swirling flow remaining in the second stage outlet region,

the recovery of this swirling flow is an issue for the improvement of performance.

The relative flow angles  $\beta_1$  and  $\beta_2$  at the outer and inner circumferences, which are obtained from the time-averaged values of  $v_r$  and  $v_u$  for the Straight and Curved Blades runners, are shown in Figures 12(a) and 12(b), respectively. The  $\beta_1$  and  $\beta_2$  values of both runners decrease as  $\theta$  increases. Observing the Curved Blades runner, it is inferred that, in the first stage inlet region,  $\beta_1$  coincides with a blade angle of  $30^\circ$  at around  $\theta = 70^\circ$ , whereas it largely diverges from the blade angle in the low- $\theta$  region, causing great shock loss. On the other hand, observing the Straight Blades runner, it is inferred that  $\beta_1$  coincides with a blade angle of  $90^\circ$  at around  $\theta = 49^\circ$ , while the flow runs almost along the blades in the region of  $\theta = 27^\circ - 57^\circ$ . Owing to the above results, it is believed that the Straight Blades runner has a small shock loss in the low- $\theta$  region at the first stage inlet region, with  $v_{r1}$  increasing, as mentioned earlier. However, in the second stage inlet region, it is thought that shock loss is large because  $\beta_2$  greatly diverges from the blade angle  $90^\circ$ .

For both Straight and Curved Blades runners, the results of experimental visualization are presented in Figures 13(a) and 13(b), while the absolute velocity vectors from numerical analyses are shown in Figures 14(a) and 14(b). Comparing the experimental and computational results, it is confirmed that the flow fields including the water depth qualitatively coincide between the two results for both runners. From both the experimental and computational results, it is reconfirmed that the upstream water depth is smaller in the case of the Straight Blades runner than in the case of the Curved Blades runner. The computed results demonstrate that the Curved Blades runner is different from the Straight Blades runner in that the Curved Blades runner has air intruding between the blades and flow turbulences occurring in the low- $\theta$  region at the first stage inlet and that it whirls up water, accompanied by counter flows occurring in the low- $\theta$  region at the first stage inlet. Furthermore, it is confirmed that the flow sharply turns against the main flow in the second stage outlet region. These conditions seem to be the causes of the loss in the Curved Blades runner.

## 5. Conclusions

Applying straight blades to an undershot cross-flow water turbine and examining its performance and flow field compared with those of the Curved Blades runner through experiments and numerical analyses showed the following results:

- (1) The output power and the turbine efficiency of the Straight Blades runner ( $\beta_{b1} = 90^\circ$ ,  $\beta_{b2} = 90^\circ$ ) were greater than those of the Curved Blades runner ( $\beta_{b1} = 30^\circ$ ,  $\beta_{b2} = 90^\circ$ ) throughout the rotational speed range. Compared with the Curved Blades runner, the output power and the turbine efficiency of the Straight Blades runner were improved by about 31.7% and about 67.1%, respectively.
- (2) The upstream water depth of the Straight Blades runner was smaller than that of the Curved Blades

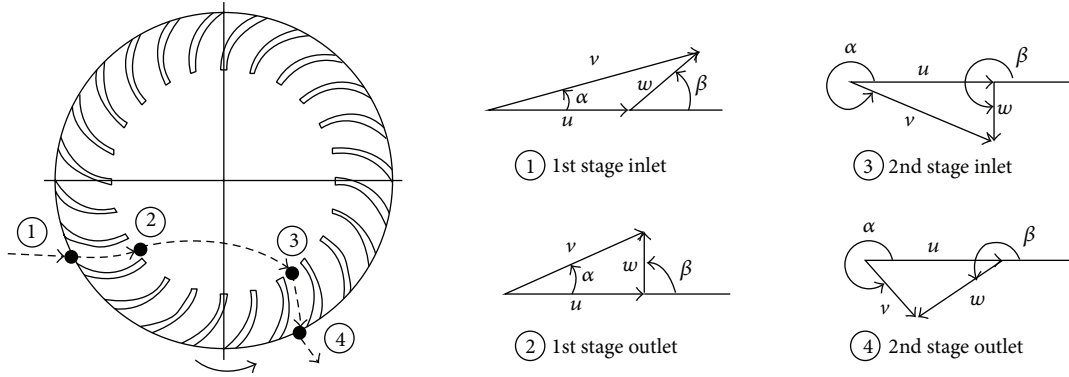


FIGURE 9: Velocity triangles at the runner inlet (points 1 and 2) and outlet (points 3 and 4).

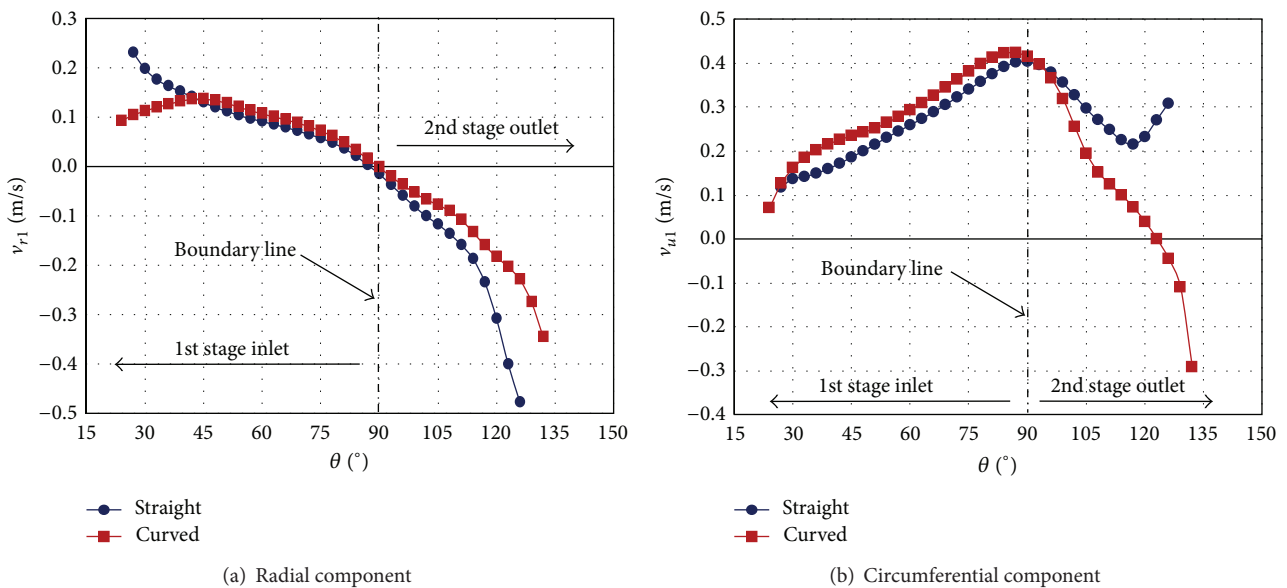


FIGURE 10: Absolute velocity at outer circumference ( $n = 22 \text{ min}^{-1}$ , cal.).

runner, whereas the downstream water depth of the Straight Blades runner was greater than that of the Curved Blades runner.

- (3) The water domains at the outer and inner circumferences of the runners were narrower on the Straight Blades runner than on the Curved Blades runner. Therefore, the first stage inlet region and second stage outlet region of the Straight Blades runner were narrower than those of the Curved Blades runner. Whereas the second stage inlet region was narrower on the Straight Blades runner than on the Curved Blades runner, the first stage outlet region was approximately the same for both runners.
- (4) Whereas the circumferential component of the absolute velocity at the high circumferential angle in the second stage outlet region was positive for the Straight Blades runner, it was negative for the Curved Blades runner. Thus, it is inferred that the flow in the

aforesaid region on the Curved Blades runner is in the direction opposite to the runner's rotation, hindering the reversal flow (including the leakage flow at the bottom) and sharply turning against the main flow.

- (5) The relative flow angle in the first stage inlet region of the Straight Blades runner coincides with a blade angle at a circumferential angle of around  $49^\circ$ , while the flow runs generally along the blades in the circumferential angle range of  $27^\circ$ – $57^\circ$ . On the other hand, the relative flow angle of the Curved Blades runner coincides with the blade angle at a circumferential angle of around  $70^\circ$ , largely diverting from the blade angle at the low circumferential angle. Consequently, at the low circumferential angle, the radial component of the absolute velocity on the Curved Blades runner decreases, whereas that on the Straight Blades runner increases.

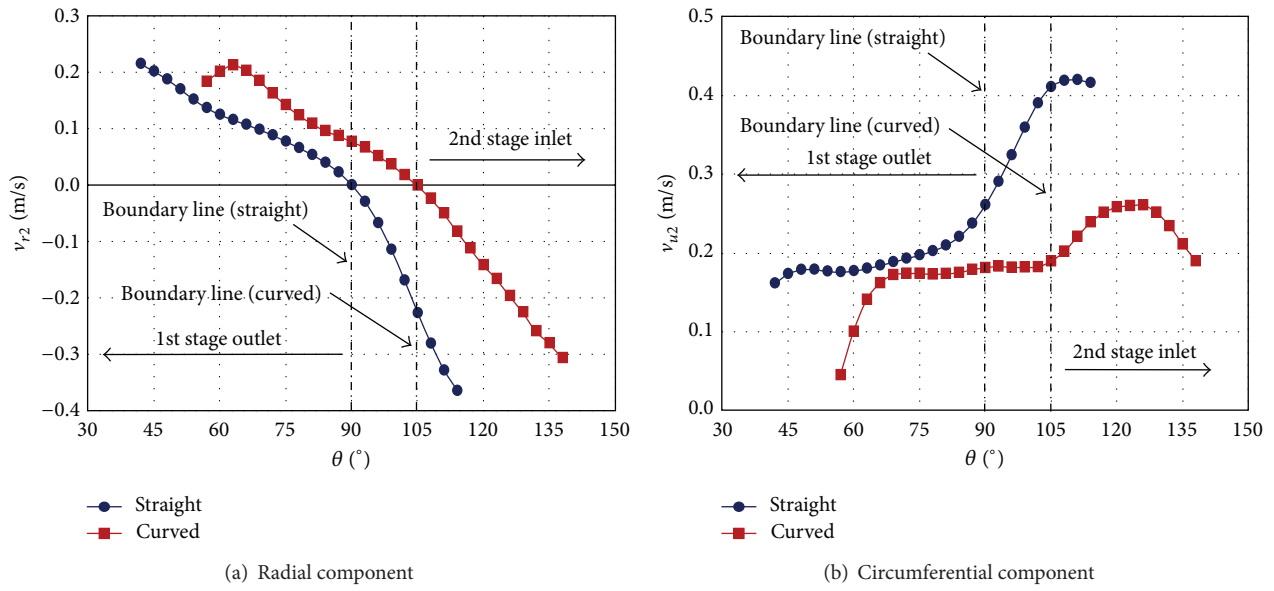


FIGURE 11: Absolute velocity at inner circumference ( $n = 22 \text{ min}^{-1}$ , cal.).

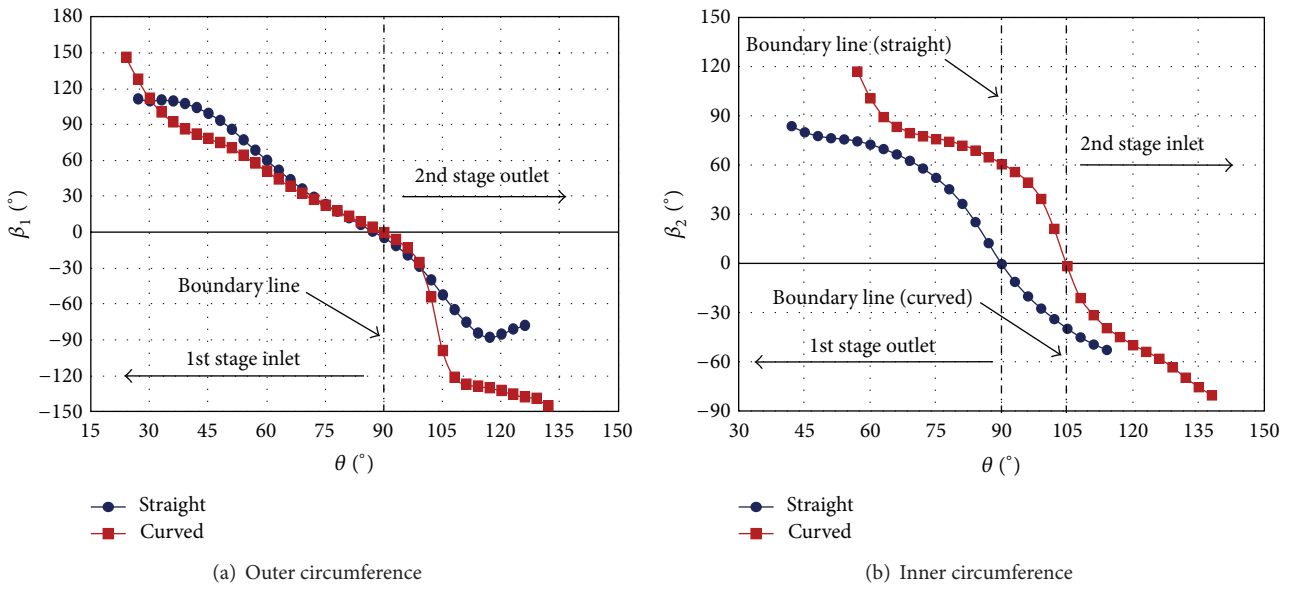


FIGURE 12: Relative flow angle ( $n = 22 \text{ min}^{-1}$ , cal.).

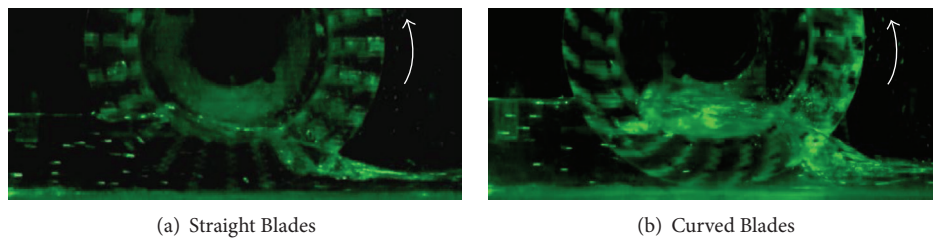


FIGURE 13: Visualization results ( $n = 22 \text{ min}^{-1}$ , exp.).

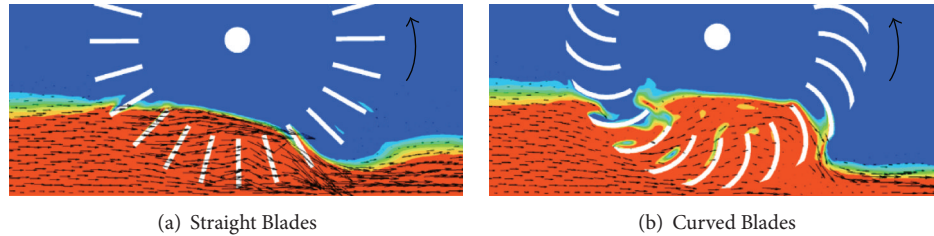


FIGURE 14: Absolute velocity vectors ( $n = 22 \text{ min}^{-1}$ , cal.).

## Nomenclature

$B$ :	Channel width m
$b$ :	Runner width m
$D$ :	Runner diameter m
$g$ :	Gravitational acceleration $\text{m/s}^2$
$H$ :	Effective head m, equal to $h_3 + v_3^2/2g - h_4 - v_4^2/2g$
$h$ :	Water depth m
$n$ :	Rotational speed $\text{min}^{-1}$
$P$ :	Output power W, equal to $2\pi nT/60$
$Q$ :	Flow rate $\text{m}^3/\text{s}$
$T$ :	Torque N·m
$u$ :	Circumferential velocity $\text{m/s}$
VF:	Volume fraction of water
$v$ :	Absolute velocity $\text{m/s}$
$w$ :	Relative velocity $\text{m/s}$
$Z$ :	Number of blades.

## Greek Letters

$\alpha$ :	Absolute flow angle $^\circ$
$\beta$ :	Relative flow angle $^\circ$
$\beta_b$ :	Blade angle $^\circ$
$\gamma$ :	Clearance between runner and side walls m
$\delta$ :	Clearance between runner and floor m
$\eta$ :	Turbine efficiency = $P/\rho gQH$
$\theta$ :	Circumferential angle $^\circ$
$\rho$ :	Fluid density $\text{kg/m}^3$ .

## Subscripts

1:	Inner circumference of runner
2:	Outer circumference of runner
3:	Upstream
4:	Downstream
$r$ :	Radial component
$u$ :	Circumferential component.

## Conflict of Interests

The authors declare that there is no conflict of interests regarding the publication of this paper.

## References

- [1] C. Nicolet, A. Zobeiri, P. Maruzewski, and F. Avellan, "Experimental investigations on upper part load vortex rope pressure fluctuations in francis turbine draft tube," *International Journal of Fluid Machinery and Systems*, vol. 4, no. 1, pp. 179–190, 2011.
- [2] T. Vu, M. Koller, M. Gauthier, and C. Deschênes, "Flow simulation and efficiency hill chart prediction for a Propeller turbine," *International Journal of Fluid Machinery and Systems*, vol. 4, no. 2, pp. 243–254, 2011.
- [3] C. Yang, Y. Zheng, and L. Li, "Optimization design and performance analysis of a pit turbine with ultralow head," *Advances in Mechanical Engineering*, vol. 2014, Article ID 401093, 7 pages, 2014.
- [4] T. S. Reynolds, *Stronger Than a Hundred Men: A History of the Vertical Water Wheel*, The Johns Hopkins University Press, Baltimore, Md, USA, 1983.
- [5] Y. Fujiwara, H. Kado, and Y. Hosokawa, "History and performance of traditional water wheel in Western Europe," *Transactions of the Japan Society of Mechanical Engineers*, vol. 90, no. 819, pp. 212–218, 1987.
- [6] A. Furukawa, S. Watanabe, D. Matsushita, and K. Okuma, "Development of ducted Darrieus turbine for low head hydropower utilization," *Current Applied Physics*, vol. 10, supplement, no. 2, pp. S128–S132, 2010.
- [7] Y. Nishi, T. Inagaki, R. Omiya, T. Tachikawa, M. Kotera, and J. Fukutomi, "Study on a cross-flow water turbine installed in an open channel," *Turbomachinery*, vol. 39, no. 8, pp. 467–474, 2011.
- [8] Y. Nishi, T. Inagaki, Y. Li, R. Omiya, and J. Fukutomi, "Study on an undershot cross-flow water turbine," *Journal of Thermal Science*, vol. 23, no. 3, pp. 239–245, 2014.
- [9] C. A. Mockmore and F. Merryfield, "The banki water turbine," *Bulletin Series 25*, 1949.
- [10] J. Fukutomi, "Characteristics and internal flow of cross-flow turbine for micro hydro power," *Turbomachinery*, vol. 28, no. 3, pp. 156–163, 2000.
- [11] Y. Nishi, T. Inagaki, R. Omiya, and J. Fukutomi, "Performance and internal flow of an undershot-type cross-flow water turbine," *Transactions of the Japan Society of Mechanical Engineers, Series B*, vol. 79, no. 800, pp. 521–532, 2013.
- [12] Y. Nishi, T. Inagaki, Y. Li, R. Omiya, and K. Hatano, "The flow field of undershot cross-flow water turbines based on PIV measurements and numerical analysis," *International Journal of Fluid Machinery and Systems*, vol. 7, no. 4, pp. 174–182, 2014.
- [13] ANSYS, *ANSYS CFX-Solver Theoretical Guide*, 2010.
- [14] ANSYS, *ANSYS CFX-Solver Modeling Guide*, ANSYS, 2010.



**Hindawi**

Submit your manuscripts at  
<http://www.hindawi.com>

